Processability of pure Zn and pure Fe by SLM for biodegradable metallic implant manufacturing

Montani, Marco; Demir, ALI GOKHAN; Mostaed, Ehsan; Vedani, Maurizio; Previtali, Barbara

Rapid Prototyping Journal

Processability of pure Zn and pure Fe by SLM for biodegradable metallic implant manufacturing
Marco Montani, Ali Gökhan Demir, Ehsan Mostaed, Maurizio Vedani, Barbara Previtali,

Article information:

Users who downloaded this article also downloaded:

![Politecnico di Milano logo] POLITECNICO DI MILANO

For Authors

If you would like to write for this, or any other Emerald publication, then please use our Emerald for Authors service information about how to choose which publication to write for and submission guidelines are available for all. Please visit www.emeraldinsight.com/authors for more information.

About Emerald www.emeraldinsight.com

Emerald is a global publisher linking research and practice to the benefit of society. The company manages a portfolio of more than 290 journals and over 2,350 books and book series volumes, as well as providing an extensive range of online products and additional customer resources and services.

Emerald is both COUNTER 4 and TRANSFER compliant. The organization is a partner of the Committee on Publication Ethics (COPE) and also works with Portico and the LOCKSS initiative for digital archive preservation.

Processability of pure Zn and pure Fe by SLM for biodegradable metallic implant manufacturing

1. Introduction

Selective laser melting is an established technology for the manufacturing of permanent biomedical devices, such as orthopaedic and dental implants (Gu *et al.* 2012). The technology also allows for the manufacturing of customized implants for specific patients. Through tomographic imaging to the implant manufacturing, the process is held in digital environment ensuring high flexibility. When moving to manufacturing, both in industry and in research, the most commonly applied materials in selective laser melting have been up to now metallic permanent bio-implant materials namely, stainless steel (Meier and Haberland, 2008; Yasa and Kruth, 2011; Kamath *et al.*, 2014), Co-Cr (Murr *et al.*, 2012; Xin *et al.*, 2012; Xin *et al.*, 2013; Song, C. *et al.*, 2014; Vandenbroucke and Kruth, 2007) and Ti alloys (Vandenbroucke and Kruth, 2007; Stamp *et al.*, 2009; Amin Yavari *et al.*, 2013; Zhang *et al.*, 2014; Song, B. *et al.*, 2012; Attar *et al.*, 2014). These materials have been used widely in prosthetic, cardiovascular implants and in general surgery due to their mechanical properties and chemical stability. One of the main concerns regarding stainless steel is the release of allergenic elements such as Ni during the slow bio-degradation process, reducing biocompatibility of the material (Witte *et al.*, 2008). Titanium alloys show higher biocompatibility properties. Biodegradability, on the other hand, refers to the ability of the material to safely dissolve in body fluids with time (Zheng *et al.*, 2014). The implant material is designed so that it can be metabolized in time due to the dissolution induced by the physiological fluid corrosion. The property is highly appealing for minimally invasive treatments, where the implant is designed to dissolve after the required duration of the treatment. For infant patients, biodegradability is essential also due to the body growth, which is not followed by the permanent implant. Hence, with biodegradability, a second surgery for implant removal can be also avoided.

Concerning biodegradable materials, polymeric (Nair and Laurencin, 2007) and metallic (Zheng *et al.*, 2014) options exist. Metallic biodegradable materials are advantageous due to their superior mechanical properties, whereas polymeric ones can be tailored more flexibly for biodegradation rate. The majority of the works on biodegradable metallic materials concerns the use of Mg and its alloys. In order to overcome the high bio-degradation rate of Mg, pure Fe and Fe-Mn alloys have been proposed recently (Moravej *et al.*, 2010;

1

Hermawan *et al.*, 2010a; Hermawan *et al.*, 2010b). A newer family of biodegradable metals recently emerged based on Zn (Yu *et al.*, 2014; Vojtěch *et al.*, 2011). Zinc is essential for the immune system and is a co-factor for specific enzymes in bone and cartilage (Zheng *et al.*, 2014). Possessing a degradation rate slower than Mg alloys and faster than Fe alloys, Zn and its alloys stand out as a promising application especially for cardiovascular stents. Besides their biological performance, the biodegradable metallic materials require a better comprehension in the manufacturing technologies. Despite the great potential of SLM in customizing biomedical implants, the studies are much more concentrated on permanent implant materials. In literature, few works concerning SLM of biodegradable metals are present, most of which are on Mg and its alloys (Ng *et al.*, 2011a; Ng *et al.*, 2011b; Wei *et al.*, 2014; Zhang *et al.*, 2012). Although several studies concerning ferrous alloys (Kruth *et al.*, 2004) are reported, only a few works on pure Fe are present (Song, B. *et al.*, 2014a; Song, B. *et al.*, 2014b). Regarding Zn and its alloys, literature lacks works also on more conventional manufacturing processes, while SLM of this material has not been reported previously to authors' knowledge.

In the meanwhile, basic research is being undertaken on the new family of biodegradable Fe and Zn alloys, concerning material properties as well as biocompatibility and degradation behaviour for applications mainly regarding cardiovascular stents, while their applicability to larger implants such as orthopaedic ones is being investigated (Bowen *et al.*, 2013; Shearier *et al.* 2016, Mostaed *et al.*, 2016; Zhu *et al.*, 2009; Moravej *et al.*, 2010; Wegener *et al.*, 2011). The use of SLM with biodegradable metals provides further advantages such as the control over material density and microstructure, by regulating part geometry and energy input to the material. Such features are important for controlling degradation behaviour and biological response of the biodegradable implant. Benefiting from these properties, the use of SLM can be used to enhance the properties of implants with standardized geometries such as screws, rods and cardiovascular clips. In order to facilitate the great potential in future uses, the processability of the new family of biodegradable metals through additive SLM has to be assessed.

Concerning the SLM of new materials, the key indicator to evaluate process feasibility is the part density. Several studies are available concerning the optimization of main process parameters, such as laser power, scan speed, hatch distance and layer thickness. Commonly, the published works avoid the study of all the parameters together, varying a couple of them and fixing the rest. Different combinations of laser power and

2

scan speed are the most commonly studied amongst the possibilities. In the published works, stainless steel and ferrous alloys appear to be processed with power levels ranging between 50 and 400 W with scan speeds starting from 50 going up to 2000 mm/s (Yasa and Kruth, 2011; Kamath *et al.*, 2014; Ng *et al.*, 2011b; Kruth *et al.*, 2004; Song, B. *et al.*, 2014a; Song, B. *et al.*, 2014b; Yadroitsev and Smurov, 2010; Dadbakhsh *et al.*, 2012). Hatch distances are linked to the laser spot dimension. It is observed that for small spots (<100 μm in diameter), hatch distance is taken larger than the spot size itself, and for larger beams (>100 μm) hatch distance is taken below the beam size (Kamath *et al.*, 2014). Layer thickness, on the other hand, is linked to the powder grain size as well as the surface quality to avoid stair effects. The layer thickness is usually set to a value higher than the average particle dimension, in particular, it has been recommended to be less than the 90th percentile of the size distribution (Karapatis and Egger, 1999; Spierings and Levy 2009). Another common approach is to study the process in terms of energy density expressed by fluence parameter. Fluence allows for an easier interpretation of the trends against the key process indicators such as part density. However, for process optimization the single parameters are required to be studied together. The diversity of the used equipment, especially the used laser source characteristics renders difficult the use of the same process parameters on different setups. Employing new prototype systems inevitably requires preliminary tests, which can be guided by experimental ranges and rules indicated by the literature. Combination of design of experiments and simple analytical models is also useful for determining process feasibility ranges for new materials.

In this work, SLM of three different metallic biomedical implant materials was studied using a prototype system. AISI 316L stainless steel represents a common biomedical permanent implant material, which lends itself well to SLM, showing no phase transformation (Meier and Haberland, 2008). The process feasibility was determined using AISI 316L. The process window for the biodegradable pure Fe and pure Zn was estimated via lumped heat capacity model. The laser melted materials were evaluated for porosity, density and mechanical properties.

2. Materials and methods

2.1 Selective laser melting system

3

A prototype SLM system operating in laboratory environment was employed for the study. A multimode fibre laser source with 1 kW maximum power (IPG Photonics YLR-1000, Cambridge, MA, USA) was coupled to a scanner head (El.En. Scan Fiber, Florence, Italy). The optical chain was composed of a 60 mm collimating lens and a 255 mm f-theta lens. In this configuration beam diameter at focal plane (d_0) was calculated as 213 μm. The main specifications of the laser system are summarized in Table 1. The powder deposition system was designed and realized for use in laboratory environment. The powder bed was actuated by using a motorised z-axis (Thorlabs L490MZ, Newton, NJ, USA) allowing progressive lowering of the bed plane during processing. For this prototype system, SLM was carried out in a gas chamber, in which Ar flow was provided at 20 Nl/min. Schematic representation of the SLM system can be seen in Figure 1.

Table 1. Main specifications of the laser system.

Figure 1. Schematic illustration of the prototype SLM system, depicting different components.

2.2 AISI 316L stainless steel, pure Fe and pure Zn powders

Commercially available powders were acquired for the study. Mean particle size was measured on the SEM pictures via image processing software, as the average length of diameters measured at 2 degree intervals and passing through the particle centroid. The gas atomized AISI 316L stainless steel powder (supplied by Cogne Acciai Speciali, Aosta, Italy) was in spherical form with 31±8 μm mean particle size, as reported in Figure 2.a. Both pure Fe and pure Zn powders were water atomized and were provided with >99.5% purity (Metalpolveri, Brescia, Italy). Iron powder was in irregular form composed of spherical particles and flakes with 41±19 μm mean particle size (see Figure 2.b), whereas the zinc powder consisted of flakes having 42±18 μm mean particle size (see Figure 2.c). The chemical compositions and the physical properties of the materials are listed in Table 2 and Table 3, respectively. Substrate materials were matched to used powders using 2 mm thick AISI 316L stainless steel, low carbon steel and pure Zn plates.

Table 2. Nominal chemical composition of the used powders (all values are expressed in wt.%).

Table 3. Physical properties of the used materials (Poweleit, 2008; Washko and Aggen, 1990; ASM International 1990).

Figure 2. SEM images of the powder raw materials: a) AISI 316L, b) pure Fe and c) pure Zn.

2.3 Characterization equipment

4

Density of the laser melted samples was measured based on Archimedes principle with a precise balance (Precisa 100A-300M, Turin, Italy). Metallographic cross-sections of the realized samples were prepared by cutting, mounting in resin and polishing. Optical microscopy images were recorded and apparent porosity was calculated on the images employing image processing software as the fraction of the total area of the pores over the total area of the deposit. The grain size of the investigated samples was measured by ASTM E112-96 standard according to the linear intercept procedure. Vickers microhardness was measured on samples with sufficiently low porosity, with 500 gr applied load (Metkon MH-3, Bursa, Turkey). For compression tests, specimens were prepared with size of 10x10x10 mm^3 and machined to achieve flat and parallel surfaces. Compression tests have been performed under dry condition, without any use of lubricant on testing plates, with constant strain rate at $\dot{\varepsilon}=10^{-3}$ s^{-1} using a hydraulic test machine (MTS Alliance RF/150, Eden Prairie, MN USA) and according to the ASTM E9-09 specifications.

3. Experimental procedure

The experimental study consisted of different phases, as illustrated in the flow chart reported in Figure 3. In the first phase, selective laser melting of AISI 316L powder was studied to identify the feasibility window. At this stage a 2-level factorial plan was applied on AISI 316L powder where i) laser power (P [W]); ii) scan speed (v [mm/s]); iii) space between adjacent scan lines, namely hatch distance (h [μm]); iv) layer thickness (t) were varied. Focal position was fixed on surface and Ar gas was supplied with 20 Nl/min flow. Samples of 5x5x1 mm were realized. Laser power levels were fixed at 200 and 300 W, as a common interval found in the literature. Scan speed (v [mm/s]) levels were set at 150 and 300 mm/s after preliminary experiments. Hatch distance levels (h [μm]) were chosen proportional to the laser spot size, particularly at 110 μm (0.51·d_0) and 130 μm (0.60·d_0). Layer thickness (t [μm]) levels were set to allow for operating around the mean grain size at 50 μm and above at 100 μm. Statistical significance level was chosen at 5%. Samples were analysed for porosity and density. The conditions generating less than 3% apparent porosity were sought. The experimental plan is summarized in Table 4.

Table 4. Details of the experimental plan used in the SLM study of AISI 316L

5

In order to estimate the process feasibility window for the two other materials, the lumped heat capacity model (Steen and Mazumder, 2010) was used, expressed as the following

$$P \cdot \eta = \rho \cdot d_0 \cdot v \cdot t \cdot \left(c_p \cdot (T_m - T_a) + L_f \right) \tag{1}$$

where c_p [J/kg·K] is the heat capacity, T_m is the melting point, L_f is the latent heat of fusion and T_a is the room temperature, η refers to absorption coefficient. The model expresses the power required to melt a single track of material with a certain volume over time. The model greatly simplifies the process with the assumption of constant thermo-physical properties and solid material. However, it is useful for parameter range estimation and for limiting the experimental range in an optimization study. From this point of view the coefficient η can be treated as an efficiency parameter accounting for all the losses related to reflectance and porous material. Assuming to a first approximation that the reflectance and solid fraction of the spread metallic powders are similar, for the given experimental setup a global efficiency parameter could be evaluated. Hence, the optimal conditions obtained with AISI 316L were used to calibrate the model unknown efficiency parameter η. Once the η was estimated, feasibility windows for pure Fe and pure Zn were estimated using the same model with the thermo-physical parameters of these materials. The feasibility range was determined for the fluence F [J/cm^2] parameter expressed as:

$$F = \frac{P}{v \cdot t} = \frac{\rho \cdot d_0 \cdot \left(c_p \cdot (T_m - T_a) + L_f \right)}{\eta} \tag{2}$$

Fluence accounts for the energy density over a single track defined by the scanned line and layer thickness. One of the main drawbacks of fluence is that it does not account for overlapping between adjacent scan lines. If the hatch spacing is relatively small compared to the beam size, the drawback related to overlapping effects might be avoided. On the other hand, same fluence values can be achieved for different power-scan speed couples, which essentially exhibit different heating and cooling cycles. This time dependent behaviour is neglected in the fluence, therefore its use can be limited in large range of parameter levels.

Another relevant parameter that can be calculated to assess the material sensitivity to the used laser power is the vaporization time t_v. According to the following equation, it is possible to compare the materials for their susceptibility to vaporization, which is another limiting factor as opposed to incomplete melting.

$$t_v = \frac{\pi}{\alpha} \cdot \left(\frac{T_v \cdot k \cdot \pi \cdot d_0^2}{8P} \right)^2 \tag{3}$$

6

The model expresses the time required to reach vaporization on surface, where k is the conductivity, α is the heat diffusivity and T_v is the vaporization temperature of the material (Steen and Mazumder, 2010).

The estimated fluence ranges were tested on pure Fe and pure Zn. At this stage, only laser power and scan speed were varied, whereas hatch distance and layer thickness were fixed with the experience coming from the results obtained on AISI 316L. Apparent porosity and density were assessed for these materials and vaporization times in this range were compared. In the final stage, mechanical characterizations consisting of hardness and compression tests were carried out on all three materials for conditions with sufficiently low porosity.

Figure 3. The flow chart of the experimental study depicting different phases.

4. Results and discussion

4.1 Feasibility window for AISI 316L and estimation of process parameters for pure Fe and pure Zn

In Figure 4 and Figure 5 the main effects and interaction plots of the response variables are demonstrated for the AISI 316L stainless steel. The main effects plots imply that the strongest influence on both porosity and density derives from laser power (P). While an increase in laser power decreases the porosity, higher values of scan speed, hatch distance and layer thickness appear to induce higher porosity. These results are coherent with the literature, depicting that an effective increase in fluence shows reduced porosity. The main effects are similar for all process parameters in the case of porosity, except hatch distance, which appears to cause slight increase in density with higher level. In Figure 4 the interaction plot suggests interactions between laser power and scan speed (P·v), laser power and layer thickness (P·t), and scan speed and layer thickness (v·t). On the other hand, no interactions are expected between the parameters in the case of density, as shown by parallel lines in each interaction block of Figure 5. The maximum porosity was 16%, and in the best conditions porosity levels lower than 1% could be achieved. Corresponding densities were between 7.87 and 6.85 g/cm^3. As seen in Figure 4 the highest (P=150 W, v=300 mm/s, h=130 μm, t= 100 μm) and lowest porosity (P=300 W, v=150 mm/s, h=100 μm, t= 50 μm) conditions refer to the two extremes of available fluence values (F=4000 J/cm^2 and F=500 J/cm^2 respectively). The results of the statistical analysis also confirm the importance of the composite parameter, fluence. Table 5 shows results of analysis of variance

7

over the process parameters and interaction. The results confirm the previous observations, where the significant parameters over the porosity are power, scan speed, thickness and their interactions. On the other hand, the same factors without their interactions are significant parameters over density as shown in Table 5. The hatch spacing was not found to be significant over the experimented region, showing that the inverse behaviour observed with porosity measurements is also insignificant. On the contrary, in literature, hatch distance has been shown to be an important parameter for reducing porosity (Zhang *et al.*, 2014; Li *et al.*, 2010). The statistical insignificance observed in this study is expected to be due to experimenting in a restricted parameter range (110-130 µm). The statistical insignificance of hatch spacing is advantageous for the applicability of fluence model for predicting the feasibility ranges of pure Fe and pure Zn.

Figure 4. a) Main effects and b) interaction plots of porosity (p) obtained on AISI 316L.

Figure 5. a) Main effects and b) interaction plots of density (ρ) obtained on AISI 316L.

Table 5. Statistical significance of SLM parameters on AISI 316L porosity (p) and density (ρ) depicted by corresponding p-values.

The acceptable condition featuring a porosity lower than 3% was found to be between $F=2000\text{-}4000$ J/cm^2. Hence, this fluence range was used to estimate the efficiency parameter η, rewriting Eq. 1. The estimated range was $\eta=0.04\text{-}0.08$. Using this efficiency parameter range, the fluence for pure Fe and pure Zn are found as $F_{Fe}=1993\text{-}3986$ J/cm^2 and $F_{Zn}=478\text{-}956$ J/cm^2. With the information gathered with AISI 316L tests, hatch spacing was fixed at 100 µm also for SLM study on pure Fe and pure Zn. Layer thickness was fixed to 50 µm, since it allows reducing porosity. On the other hand, power levels were chosen at 200 and 300 W, whereas scan speeds were varied to respect the estimated fluence ranges. For pure Fe the scan speed range was selected between 150 and 300 mm/s, whereas for pure Zn it varied between 600 and 1900 mm/s. The resultant fluence ranges results therefore to be larger than the predicted ones as depicted in Figure 6. The experimental conditions for pure Fe and pure Zn are summarized in Table 4. All conditions were replicated twice. The vaporization time of pure Zn appears to be much lower than AISI 316L and pure Fe as seen in Figure 6. In particular, pure Zn is expected to evaporate approximately 4 time faster than pure Fe and twice as fast as AISI 316L.

8

Figure 6. a) Predicted and used fluence ranges for the experimented powders and b) vaporization times as a function of laser power.

Table 6. Details of the experimental plan used in the SLM study of pure Fe and pure Zn.

4.2 SLM of pure Fe and pure Zn

Representative micrographs of laser melted pure Fe and pure Zn powders belonging to low and high fluence values are reported in Figure 7. It can be seen that the fluence region provided by the lumped heat capacity model was effective in predicting process parameter window. The deposited materials obtained with low fluence levels resulted in high porosity for all materials. Laser melted pure Fe was characterized by 2.5% apparent porosity with the highest fluence at 4000 J/cm^2, whereas the highest apparent porosity was 7.9% with the lowest fluence at 1333 J/cm^2. Pure Zn exhibited lower processability and higher porosity in general. Due to the low vaporization temperature, obtained deposits were always characterized by porosity higher than 12%. Moreover, at 300 W laser power, the process was found to be less stable due to more pronounced material loss due to vaporization. The significant porosity observed in laser melted Zn samples generates a foam-like structure. The measured porosity and density of the laser melted materials as a function of fluence are reported in Figure 8. For both response variables, regression models with power function were found to be suitable. All models fitted the data very well as can be observed in the related plots and without lack-of-fit as confirmed by the statistical tests. This confirmed that the use of fluence in the experimented range is appropriate, especially for AISI 316L and pure Fe, despite the fact that it neglects the time dependent process characteristics. For pure Zn, the fluence model could be applied to the experimented range with only 200 W laser power, showing the limit of this approach for a material with low vaporization temperature. The density values show that full density products with laser melted pure Fe ($\rho_{max,Fe}$=7.82 g/cm^3) and AISI 316L ($\rho_{max,316L}$=7.87 g/cm^3) can be achieved. The high porosity of laser melted Zn also reduces its density, thus the achieved density was much lower than the nominal value ($\rho_{max,Zn}$=6.10 g/cm^3). Further increase of the fluence by reducing the scan speed resulted in no improvement, since the process was vaporization dominant. Moreover, the gaseous phase might generate melt pool instabilities, resulting in higher porosity (Qiu et al, 2015). It is expected that, porosity can be further reduced by the use of different laser melting strategies, employing pulsed emission to better manage the applied heat cycle. Another important factor is the powder shape and manufacturing method. Water atomized particles are reported to induce higher

porosity due to the reduced packing and higher oxygen content, even with alloys with high melting temperature (Li *et al.*, 2010; Engeli *et al.*).

Figure 7. Laser melted layers obtained in high and low fluence conditions showing porosity: a) AISI 316L at F=4000 J/cm², b) AISI 316L at F=500 J/cm², c) pure Fe at F=4000 J/cm², d) pure Fe at F=1333 J/cm², e) pure Zn at F=667 J/cm², f) pure Zn at F=211 J/cm².

Figure 8. a) Porosity (p) and b) density (ρ) as a function of employed fluence.

4.3 Material characterization

Figure 9 shows the microstructures of the laser melted materials. Very fine cellular-dendritic microstructure is observed on AISI 316L, generated due to the rapid cooling cycles induced by the laser beam. The microstructure of the pure Fe shows fine grains with an average size of 5.5 μm. In addition to the high porosity, a significantly fine grain structure can be observed in the laser melted Zn samples (see Figure 9.c).

Figure 9. Microstructures of lase melted a) AISI 316L, b) pure Fe, and c) pure Zn.

The mechanical properties of the laser melted powders are presented in Figure 10. The compressive yield stress and micro-hardness (HV) of laser melted samples are compared to their as-cast, and wrought counterparts. For comparison, reference data was used for AISI 316L and low carbon steel for the case of pure Fe (Poweleit, 2008; Washko and Aggen, 1990). For Zn, experimental tests were carried out according to same procedures on cast ingots (99.995% purity, Gerli Metalli, Milan, Italy), which were also used for the wrought Zn samples, prepared by extrusion.

Laser melted AISI 316L showed higher compression yield stress (CYS) and HV compared to the conventionally produced material with CYS=372±15 MPa and 245±6 HV. Pure Fe showed mechanical properties fully comparable to a low carbon steel with CYS=197±18 MPa and 150±5 HV. Laser melting produced improved CYS on Zn as opposed to as-cast and wrought material owing to refined grain structure, with CYS=99±22 MPa. Yu et al (2014) showed that by sintering pure Zn they could achieve a CYS of 79 MPa. In the work of these authors, the fully dense sintered structure featured a grain size of approximately 450 μm. The laser melted Zn produced here, despite the high porosity showed improved mechanical

properties, which is attributed to its considerably smaller grain size. The as-cast reference samples were characterized by mm-sized grains with CYS=30 MPa, whereas in extruded samples, the average grain size was found to be 48 μm and CYS=76 MPa. In case of the laser melted Zn samples, a significantly fine lamellar-like structure with no preferential orientation was found (see the inset of Figure 9.c). The formation of such a structure is expected to be due to high magnitude of cooling rate overheat with respect to the Zn melting temperature (693 K).

Figure 10. a) Compression yield strength and b) microhardness of the laser melted AISI 316L, pure Fe and pure Zn.

5. Conclusions

In this work, a methodological study for SLM of Zn and Fe, of particular interest as biodegradable metallic materials, is proposed. The industrial standard AISI 316L stainless steel was used for process development using a prototype SLM system and for comparison of material processability. The lumped heat capacity model was used to estimate the processing range of the biodegradable metals pure Fe and pure Zn. The model satisfactorily indicated the feasibility zones, reducing a long run of experimental study. It was confirmed that AISI 316L possesses high processability in SLM process and pure Fe behaves quite similarly. Low porosity and high density deposits were achieved on Fe based powders by increasing the laser fluence. SLM of Zn is demonstrated for the first time in this work. The results suggest that pure Zn shows less processability due to its low vaporization point, generating high levels of porosity. The laser melted Zn showed mechanical strength higher than as-cast material despite 12% porosity and 86% nominal density. The improved mechanical strength is attributed to the small grain size of the material obtained through the very fast cooling cycle, induced by the laser process.

The results confirm the viability of the SLM process also for biodegradable metals, Fe and Zn. Further studies will be dedicated to the improvement of density of laser melted Zn, biodegradation and material-cell interaction to give a better perception to biomedical implant designers and manufacturers.

11

References

Amin Yavari, S., Wauthle, R., Van Der Stok, J., Riemslag, A. C., Janssen, M., Mulier, M., Kruth, J. P., Schrooten, J. , Weinans, H. and Zadpoor, A.A. (2013) "Fatigue behavior of porous biomaterials manufactured using selective laser melting," Mater. Sci. Eng. C, vol. 33, no. 8, pp. 4849–4858.

ASM International (1990), Properties of Pure Metals, "Properties and Selection: Nonferrous Alloys and Special-Purpose Materials", *ASM Handbook*, Vol 2.

ASTM E112-96 (2004), Standard Test Methods for Determining Average Grain Size, ASTM International, West Conshohocken, PA.

ASTM E9-09 (2009), Test Methods of Compression Testing of Metallic Materials at Room Temperature, Annual book of ASTM standards, ASTM, Philadelphia, PA.

Attar, H., Calin, M., Zhang, L. C., Scudino, S. and Eckert, J. (2014), "Manufacture by selective laser melting and mechanical behavior of commercially pure titanium," Mater. Sci. Eng. A, vol. 593, pp. 170–177

Bowen, P. K., Drelich, J. and Goldman, J. (2013). "Zinc exhibits ideal physiological corrosion behavior for bioabsorbable stents." *Adv. Mater.*, vol. 25, no. 18, pp. 2577-2582.

Dadbakhsh S., Hao L. and Sewell N. (2012) "Effect of selective laser melting layout on the quality of stainless steel parts," *Rapid Prototyp J,* vol. 18, pp. 241–249

Engeli R., Etter T., Hövel S. and Wegener K., (2016). "Processability of different IN738LC powder batches by selective laser melting," *J. Mater. Process. Technol.*, vol. 229, pp. 484–491

Gu, D. D., Meiners, W., Wissenbach, K. and Poprawe, R. (2012), "Laser additive manufacturing of metallic components: materials, processes and mechanisms," Int. Mater. Rev., vol. 57, no. 3, pp. 133–164

Hermawan, H., Dubé, D. and Mantovani, D. (2010), "Degradable metallic biomaterials: Design and development of Fe-Mn alloys for stents," J. Biomed. Mater. Res. A, vol. 93, no. 1, pp. 1–11.

Hermawan, H., Purnama, A., Dube, D., Couet, J. and Mantovani, D. (2010), "Fe-Mn alloys for metallic biodegradable stents: Degradation and cell viability studies," Acta Biomater., vol. 6, no. 5, pp. 1852–1860.

Kamath, C., El-Dasher, B., Gallegos, G. F., King, W. E. and Sisto, A. (2014), "Density of additively-manufactured, 316L SS parts using laser powder-bed fusion at powers up to 400 W," Int. J. Adv. Manuf. Technol., vol. 74, no. 1-4 pp. 65–78, 2014.

Karapatis N. and Egger G., (1999) "Optimization of powder layer density in selective laser sintering," *Proc. Solid Free. Fabr. Symp.*, pp. 255–264,

Kruth, J. P., Froyen, L., Van Vaerenbergh, J., Mercelis, P., Rombouts, M. and Lauwers, B. (2004), "Selective laser melting of iron-based powder," *J. Mater. Process. Technol.*, vol. 149, no. 1–3, pp. 616–622.

Li R., Shi Y., Wang Z., Wang L., Liu J. and Jiang W., (2010) "Densification behavior of gas and water atomized 316L stainless steel powder during selective laser melting," *Appl. Surf. Sci.*, vol. 256, no. 13, pp. 4350–4356.

Meier, H. and Haberland, C. (2008), "Experimental studies on selective laser melting of metallic parts," Materwiss. Werksttech., vol. 39, no. 9, pp. 665–670

Moravej, M., Prima, F., Fiset, M. and Mantovani, D. (2010), "Electroformed iron as new biomaterial for degradable stents: Development process and structure-properties relationship," Acta Biomater., vol. 6, no. 5, pp. 1726–1735.

Mostaed, E., Sikora-Jasinska M., Mostaed A., Loffredo S., Demir A.G., Previtali B., Mantovani D., Beanland R. and Vedani M. (2016), "Novel Zn-based alloys for biodegradable stent applications: Design, development and in vitro degradation." *J. Mech. Behav. Biomed. Mater.,* vol. 60, pp. 581-602.

Murr, L. E., Gaytan, S. M., Ramirez, D. A., Martinez, E., Hernandez, J., Amato, K. N., Shindo, P. W., Medina, F. R. and Wicker, R. B. (2012), "Metal Fabrication by Additive Manufacturing Using Laser and Electron Beam Melting Technologies," *J. Mater. Sci. Technol.*, vol. 28, no. 1, pp. 1–14

Nair L. S. and Laurencin C. T. (2007), "Biodegradable polymers as biomaterials," *Prog. Polym. Sci.*, vol. 32, no. 8–9, pp. 762–798.

Ng, C. C., Savalani, M. M. and Man, H. C. (2011a), "Fabrication of magnesium using selective laser melting technique," Rapid Prototyp. J., vol. 17, no. 6, pp. 479–490, 2011.

Ng, C. C., Savalani, M. M., Lau, M. L. and Man, H. C. (2011b), "Microstructure and mechanical properties of selective laser melted magnesium," *Appl. Surf. Sci.*, vol. 257, no. 17, pp. 7447–7454.

Poweleit, D. (2008) "Steel Castings Properties, Casting"*, ASM Handbook,* Vol 15, Online edition, ASM International

Qiu C., Panwisawas C., Ward M., Basoalto H. C., Brooks J. W. and Attallah M. M., (2015) "On the role of melt flow into the surface structure and porosity development during selective laser melting," *Acta Mater.*, vol. 96, pp. 72–79.

S. Zhang, Q. Wei, L. Cheng, S. Li and Y. Shi, (2014) "Effects of scan line spacing on pore characteristics and mechanical properties of porous Ti6Al4V implants fabricated by selective laser melting," *Mater. Des.*, vol. 63, pp. 185–193.

Shearier, E., Bowen, P. K., He, W., Drelich, A., Drelich, J., Goldman, J. and Zhao, F. (2016). "In Vitro Cytotoxicity, Adhesion, and Proliferation of Human Vascular Cells Exposed to Zinc" *ACS Biomater. Sci. Eng.*, vol. 2, no., pp. 634-642.

Song, B., Dong, S., Zhang, B., Liao, H. and Coddet, C. (2012) "Effects of processing parameters on microstructure and mechanical property of selective laser melted Ti6Al4V," Mater. Des., vol. 35, pp. 120–125.

Song, B., Dong, S., Deng, S., Liao, H. Coddet, C. (2014a), "Microstructure and tensile properties of iron parts fabricated by selective laser melting," *Opt. Laser Tech.*, vol.56, pp. 451–460.

Song, B., Dong, S., Deng, S., Liao, H. and Coddet, C. (2014b), "Vacuum heat treatment of iron parts produced by selective laser melting: Microstructure, residual stress and tensile behavior," *Mater. Design,* vol. 54 pp. 727–733.

Song, C., Yang, Y., Wang, Y., Wang, D. and Yu J. (2014), "Research on rapid manufacturing of CoCrMo alloy femoral component based on selective laser melting," Int. J. Adv. Manuf. Technol., vol. 75, no. 1–4, pp. 445–453

Spierings A.B. and Levy G., (2009) "Comparison of density of stainless steel 316L parts produced with selective laser melting using different powder grades," in *Proc. of Solid Freeform Fabrication Symposium*, pp. 342–353.

Stamp, R., Fox, P., O'Neill, W., Jones, E. and Sutcliffe, C. (2009), "The development of a scanning strategy for the manufacture of porous biomaterials by selective laser melting," J. Mater. Sci. Mater. Med., vol. 20, no. 9, pp. 1839–1848.

Steen, W. and Mazumder, J. (2010) *Laser material processing*, 4th edn, Springer, London

Vandenbroucke, B. and Kruth, J.-P. (2007), "Selective laser melting of biocompatible metals for rapid manufacturing of medical parts," Rapid Prototyp. J., vol. 13, no. 4, pp. 196–203.

Vojtěch, D., Kubásek, J., Šerák, J. and Novák, P. (2011) "Mechanical and corrosion properties of newly developed biodegradable Zn-based alloys for bone fixation," Acta Biomater., vol. 7, no. 9, pp. 3515–3522.

Washko, D. and Aggen, G. (1990) "Wrought Stainless Steels, Properties and Selection: Irons, Steels, and High-Performance Alloys", *ASM Handbook*, Vol 1, ASM International

Wegener, B., Sievers, B., Utzschneider, S., Müller, P., Jansson, V., Rößler, S., Nies, B., Stephani, G., Kieback, B. and Quadbeck, P. (2011) "Microstructure, cytotoxicity and corrosion of powder-metallurgical iron alloys for biodegradable bone replacement materials" *Mat. Sci. Eng. B,* vol. *176, no.* 20, pp. 1789-1796.

Wei, K., Gao, M., Wang, Z. and Zeng, X. (2014), "Effect of energy input on formability, microstructure and mechanical properties of selective laser melted AZ91D magnesium alloy," Mater. Sci. Eng. A, vol. 611, pp. 212–222.

Witte, F., Hort, N., Vogt, C., Cohen, S., Kainer, K. U., Willumeit R. and Feyerabend F. (2008), "Degradable biomaterials based on magnesium corrosion," *Curr. Opin. Solid State Mater. Sci.*, vol. 12, no. 5–6, pp. 63–72

Xin, X. Z., Chen, J., Xiang, N. and We,i B. (2013), "Surface Properties and Corrosion Behavior of Co-Cr Alloy Fabricated with Selective Laser Melting Technique," Cell Biochem. Biophys., vol. 67, no. 3, pp. 983–990.

Xin, X. Z., Xiang, N., Chen J. and Wei, B. (2012), "In vitro biocompatibility of Co-Cr alloy fabricated by selective laser melting or traditional casting techniques," Mater. Lett., vol. 88, pp. 101–103.

Yadroitsev I. and Smurov I. (2010) "Selective laser melting technology: from the single laser melted track stability to 3D parts of complex shape". Phys Procedia, vol. 5, pp. 551–560

Yasa, E. and Kruth, J. P. (2011), "Microstructural investigation of selective laser melting 316L stainless steel parts exposed to laser re-melting," Procedia Eng., vol. 19, pp. 389–395,

Yu, M., George, C., Cao, Y., Wootton, D. and Zhou, J. (2014), "Microstructure, corrosion, and mechanical properties of compression-molded zinc-nanodiamond composites," J. Mater. Sci., vol. 49, no. 10, pp. 3629–3641.

Zhang, B., Liao, H. and Coddet, C. (2012) "Effects of processing parameters on properties of selective laser melting Mg–9%Al powder mixture," Mater. Des., vol. 34, pp. 753–758.

Zhang, S., Wei, Q., Cheng, L., Li, S. and Shi, Y. (2014), "Effects of scan line spacing on pore characteristics and mechanical properties of porous Ti6Al4V implants fabricated by selective laser melting," Mater. Des., vol. 63, pp. 185–193

Zheng, Y. F., Gu, X. N. and Witte, F. (2014), "Biodegradable metals," *Mater. Sci. Eng. R Reports*, vol. 77, pp. 1–34.

Zhu, S., Huang, N., Xu, L., Zhang, Y., Liu, H., Sun, H. and Leng, Y. (2009). Biocompatibility of pure iron: in vitro assessment of degradation kinetics and cytotoxicity on endothelial cells. *Mater. Sci. Eng. C*, vol. *29, no.* 5, pp.1589-1592.

Table 1. Main specifications of the laser system.

Wavelength	λ	1070 nm
Beam parameter product	BPP	1.7
Beam quality factor	M^2	5.14
Maximum power	P	1000 W
Fibre diameter	d_f	50 μm
Focal distance of collimating lens	f_c	60 mm
Focal distance of focusing lens	f_f	255 mm
Beam diameter at focal plane	d_0	213 μm

Table 2. Nominal chemical composition of the used powders (all values are expressed in wt.%).

Material	C	Si	Cr	Ni	Mo	Mn	Cd	S	O	Fe	Zn
AISI 316L	<0.03	0.5	17	12	2.5	1.5				bal.	
Pure Fe								≤0.01	≤0.01	bal.	
Pure Zn							0.03				bal.

Table 3. Physical properties of the used materials (Poweleit, 2008; Washko and Aggen, 1990; ASM International 1990).

Material	ρ [kg/m^3]	c_p [J/kg·K]	k [W/m·K]	α [m^2/s]	T_m [K]	L_f [kJ/kg]	T_v [K]
AISI 316L	8000	500	20	$5 \cdot 10^{-6}$	1723	260	3273
Pure Fe	7870	447	50	$14 \cdot 10^{-6}$	1811	275	3273
Pure Zn	7133	382	113	$43 \cdot 10^{-6}$	693	101	1180

Table 4. Details of the experimental plan used in the SLM study of AISI 316L.

Varied parameters	
Power, P [W]	150, 300
Scan speed, v [mm/s]	150, 300
Hatch spacing, h [μm]	100, 130
Layer thickness, t [μm]	50, 100
Fixed parameters	
Focal position, Δz [mm]	0
Gas	Ar at 20 Nl/min

Table 5. Statistical significance of SLM parameters on AISI 316L porosity (p) and density (ρ) depicted by corresponding p-values.

Source	p	ρ [g/cm^3]
P [W]	**0.001**	**0.008**
v [mm/s]	**0.003**	**0.008**
h[μm]	0.237	0.406
t[μm]	**0.010**	**0.016**
P [W]*v [mm/s]	**0.015**	0.796
P [W]*h [μm]	0.548	0.435
P [W]*t [μm]	**0.036**	0.977
v [mm/s]*h [μm]	0.248	0.620
v [mm/s]*t [μm]	**0.036**	0.832
h[μm]*t [μm]	0.986	0.687

Table 6. Details of the experimental plan used in the SLM study of pure Fe and pure Zn.

	Pure Fe	Pure Zn
Varied parameters		
Power, P [W]	200, 300	200, 300
Scan speed, v [mm/s]	150, 200, 250, 300	600, 750, 900, 1050, 1300, 1500, 1700, 1900
Fixed parameters		
Hatch spacing, h [μm]	100	100
Layer thickness, t [μm]	50	50
Focal position, Δz [mm]	0	0
Gas	Ar at 20 Nl/min	Ar at 20 Nl/min
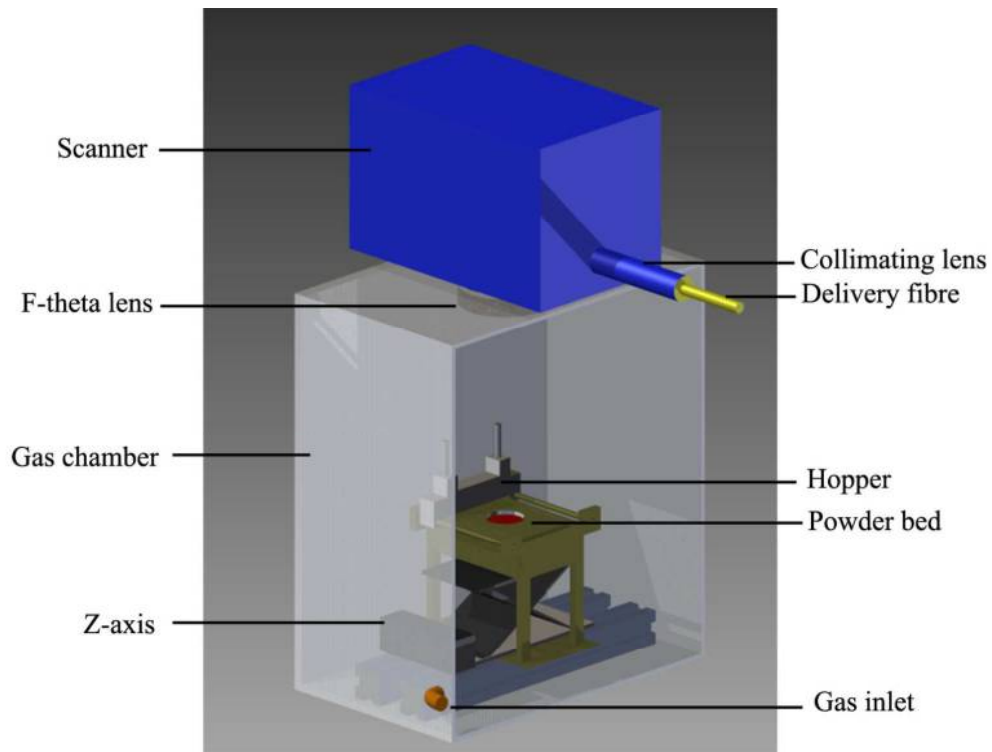
Figure 1. Schematic illustration of the prototype SLM system, depicting different components.
Figure 1
523x390mm (72 x 72 DPI)
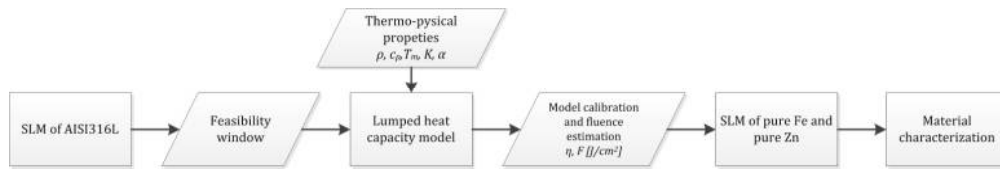
Figure 3. The flow chart of the experimental study depicting different phases.
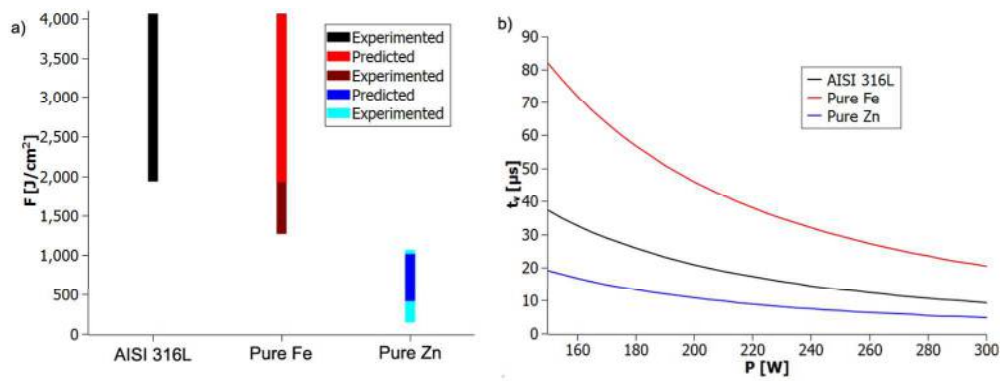Figure 3
205x33mm (300 x 300 DPI)

Figure 6. a) Predicted and used fluence ranges for the experimented powders and b) vaporization times as a function of laser power.
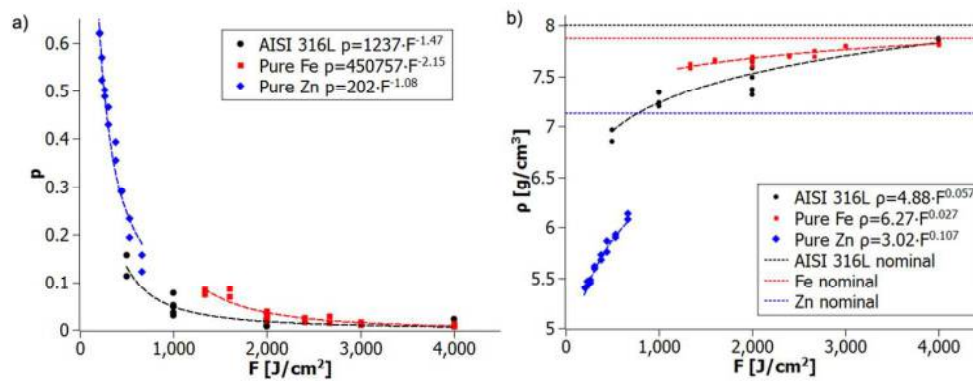Figure 6
533x200mm (72 x 72 DPI)

Figure 8. a) Porosity (p) and b) density (ρ) as a function of employed fluence.
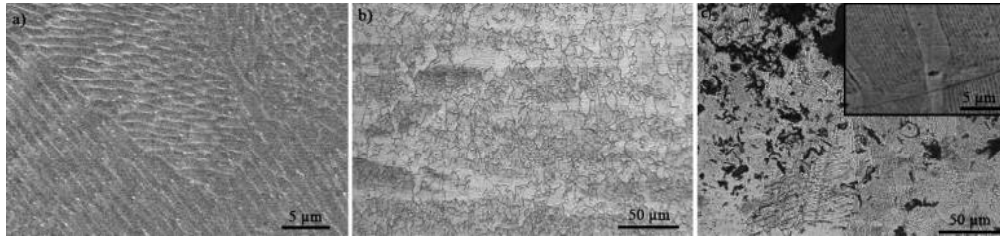Figure 8
484x190mm (72 x 72 DPI)

Figure 9. Microstructures of lase melted a) AISI 316L, b) pure Fe, and c) pure Zn.
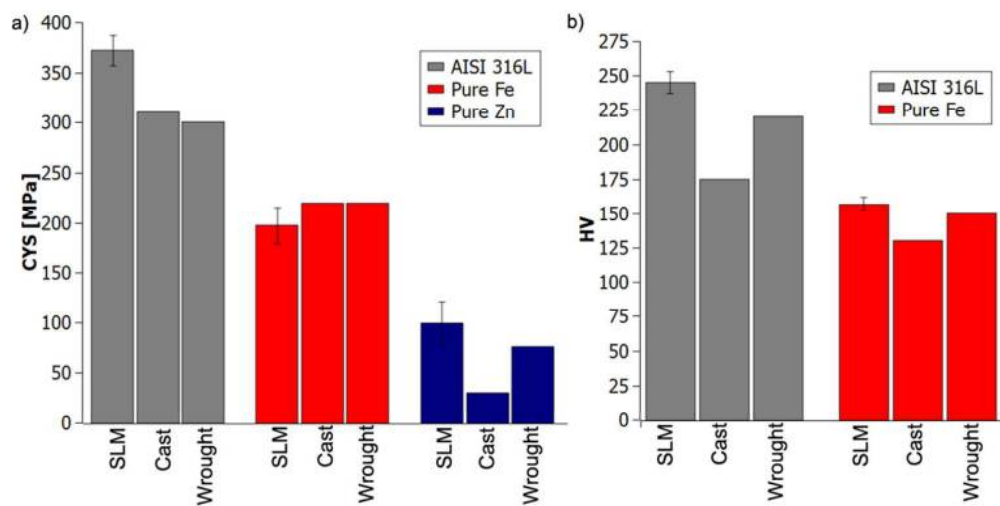Figure 9
155x36mm (300 x 300 DPI)

Figure 10. a) Compression yield strength and b) microhardness of the laser melted AISI 316L, pure Fe and pure Zn.
Figure 10
457x230mm (72 x 72 DPI)